Soil Dynamics and Earthquake Engineering 179 (2024) 108560

Contents lists available at ScienceDirect

Soil Dynamics and Earthquake Engineering

journal homepage: www.elsevier.com/locate/soildyn

High-speed railway-induced ground and building vibration: Numerical validation of a spectral element analysis-based sub-model method

Duo Feng [a,*], Roberto Paolucci [a], Ilario Mazzieri [b], Linrong Xu [c], Yu Cai [d]

[a] Department of Civil and Environmental Engineering, Politecnico di Milano, Milan, Italy
[b] MOX - Modelling and Scientific Computing, Department of Mathematics, Politecnico di Milano, Milan, Italy
[c] School of Civil Engineering, Central South University, Changsha, People's Republic of China
[d] College of Water Resources and Civil Engineering, Hunan Agricultural University, Changsha, People's Republic of China

ARTICLE INFO

Keywords:
Train-induced vibration
Structure dynamics
Equivalent section estimation
Spectral element analysis

ABSTRACT

This paper proposes a spectral element method-based analysis procedure to study further the low-frequency responses of the ground and building induced by high-speed railways. Based on an existing scale model building test in Portugal, the properties of the track–ground submodel are calibrated to determine the moving perturbation on the ground surface. In modeling the soil–structure coupled subsystem, multi-objective optimization is employed to estimate the equivalent structural properties to mitigate computational inefficiency when using continuum elements. The accuracy of the numerical prediction is compared with the experimental records at several monitoring points in terms of ground and floor slab vertical vibrations induced by two types of high-speed trains. In addition to the analysis of possible factors related to systematic discrepancies, special attention is paid to investigating the influence of (a) the presence of frame structure as well as (b) the vehicle properties on ground motion in this particular case.

1. Introduction

Although high-speed railways (HSR) have increasingly become popular worldwide, the increasing vibrations and noise generated by HSR adversely affect nearby residents [1,2] and sensitive facilities [3], making it essential to improve the accuracy of predictive tools of vibrations in structures close to the railways [4–6]. The typical prediction involves three parts: (a) the railway structure, (b) the ground, and (c) the buildings. Each one has distinct characteristics that pose challenges to coupled analyses including all such parts, due to their different spatial scales. As a result, to reduce the computational demand, reduced formulations of the problem were developed, such as by taking advantage of sub-structuring approaches [7].

Early approaches were primarily conducted using simple analytical or empirical methods. Waller et al. [8] investigated building vibrations to the train passages using the Single-Degree-Of-Freedom (SDOF) model. More detailed models, including non-building components, were proposed later. Hunt et al. [9,10] introduced a vehicle–ground model to predict the building vibrations induced by underground trains. Balendra et al. [11] investigated the 2D response of coupled tunnel–soil-SDOF models.

Many studies have pointed out the role of SSI (Soil–Structure Interaction) in practical applications. Among them, Fiala et al. [12] validated a sub-model method for predicting surface railway-induced vibrations. Connolly et al. [13] studied the additional ground and building vibrations caused by railway defects, where the responses of the soil–building model were calculated based on the free field. This decoupled strategy has also been featured in recent analytical studies. Sanayei et al. [14] and Zou et al. [15] developed the impedance model method and predicted column responses through foundation vibrations.

A fully coupled analysis was conducted by Pyl et al. [16,17] to assess truck-induced building vibrations. Coulier et al. [18] later modified Pyl's model to examine the source-receiver interaction effect, indicating that coupling effects could be disregarded when the building–railway distance exceeds several times the dominant wavelengths. However, this conclusion was based on an average indicator (mean power flow), and response differences still existed within and around buildings. These observations suggest that accurate numerical predictions depend on (1) the efficiency of the numerical formulation and (2) the simplification strategy towards the ground–building system.

To address them, in this paper we utilize the Spectral Element Method (SEM), enhanced by a Discontinuous Galerkin (DG) approach to improve the SEM flexibility in handling non-conforming sub-models of different size. The SEM formulation adopted in this work was first devised in the 1990s for elastodynamic problems [19], by coupling the

* Corresponding author.
E-mail address: duo.feng@polimi.it (D. Feng).

https://doi.org/10.1016/j.soildyn.2024.108560
Received 27 July 2023; Received in revised form 16 January 2024; Accepted 20 February 2024
Available online 23 February 2024

Table 1
The operating speed, axle loads, and spacings of Alfa Pendular and Intercity vehicles [30].

Types of trains/Operating speed		Alfa Pendular/219 km/h						Intercity/205 km/h	
Vehicle		BAS	BBS	RNB	RNH	BBN	BAN	BS 5600	Corail
Axle load [kN]	1	129.8	131.4	128.8	132.6	133.2	130.2	213.4	117.7
	2	133.2	134.8	128.8	132.6	136.6	133.6		
	3	132.6	134.8	128.8	132.6	136.6	134.2		
	4	129.2	131.4	128.8	132.6	133.2	130.8		
Interval [m]	1–2	2.7						3.0	2.56
	2–3	16.3						7.5	15.44
	3–4	2.7						3.0	2.56
	4–1	5.2						6.35	5.8

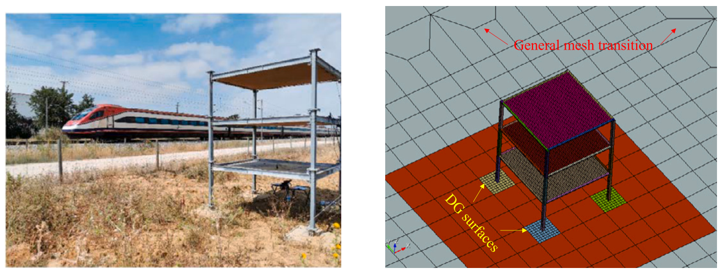

(a) (b)

Fig. 1. (a) the model building (1:3 scale) experiment [30]; (b) the related spectral element model with non-conforming mesh formulated by discontinuous Galerkin method (Section 3.3).

Lagrange polynomials with the Legendre–Gauss–Lobatto integration rule, that allowed one to achieve the flexible geometry discretization of the Finite Element Method (FEM) with preservation of spectral accuracy. After its introduction to seismic wave propagation in 3D heterogeneous media [20,21], successful validations of train-induced ground motion predictions were conducted for Sweden [22] and Belgium [23] case studies. Regarding building vibration prediction using SEM, only limited investigations were performed on the influence of urban trains on the floor slab responses [24]. Recently, the DG method has been underscored [25,26] since it allows one to account for the site-city effect by introducing the non-conforming SEM formulation [27–29].

As a foundational step towards a validation of region-scale prediction of train-induced ground response and interaction with buildings, this study takes advantage of an existing field test in which a model building is located near a railway stretch in Portugal [30,31]. Numerical simulations are carried out by SPEED [25], a high-performance parallel SEM code developed at Politecnico di Milano. In Section 2, detailed information is provided related to the site and experimental configuration. Subsequently, Section 3 presents the modeling approach, including train load determination and equivalent building estimation. After introducing the numerical non-conforming SEM model, Section 4 compares numerical results with records and provides a sensitivity study on the impact of SSI and vehicle properties. Finally, some conclusive remarks are provided.

2. Site and tests

2.1. Case study

The numerical validation refers to two experimental studies conducted at a ballasted stretch in Carregado, Portugal [30,31]. The mixed-use operating pattern makes this location suitable for train-induced environmental vibration research [32–36]. The field test records covered ground [31] and building vibrations [30] to three types of train passages. Two of them were employed in this study, traveling with speed over 200 km/h. Table 1 lists the related vehicle properties. The Intercity locomotive has higher axle loads and shorter distances between the bogies than the Alfa Pendular at a similar operating speed.

Table 2
Soil profiles and material properties based on the experimental work [31].

Layer	Thickness [m]	N_{SPT}	Mass density ρ [kg/m^3]	V_s [m/s]	V_p [m/s]	Damping ratio η
1	2.00	4	1552 (1500)	118	410	0.08
2	2.00	13	1634 (1600)	118	1072	0.04
3	4.00	18	1658 (1600)	118	1072	0.03
4	4.00	15	1965 (1900)	212	1503	0.03
5	31.5	15	1965 (1900)	302	1503	0.03

2.2. Ground and building

Soil material properties were characterized by cross-hole and spectral analysis of surface wave experiments [31]. The processed coefficients, including elastic wave speed, soil profile, etc., are detailed in Table 2, indicating that the groundwater table may be located at a depth in the range 4–8 m. Based on the statistical correlation of fine-grained soil [37] (Eq. (1)) between bulk/dry density ρ_w/ρ_d and shear wave speed V_s or N values of SPT (Standard Penetration Test), Table 2 lists the estimated and adopted (in brackets) mass density values.

$$\rho_d = 0.981 V_s^{0.090} \quad \text{or} \quad 1.46 N_{SPT}^{\;0.044}, \qquad (1)$$
$$\rho_w = 0.742 V_s^{0.166} \quad \text{or} \quad 1.67 N_{SPT}^{\;0.060}.$$

A 1:3 scale model building, as shown in Fig. 1(b), was positioned 21.2 m away from the track. This model was made of thin-walled steel beams and fiberboard [38], as detailed in Table 3. Bolts rigidly connected the structural components to simulate the actual working conditions. The field modal test indicated that its primary bending mode frequencies clustered around 15 Hz [38].

2.3. Monitoring configurations

Before and after the building construction, two monitoring plans were conducted. Initially, ground motion along the line perpendicular to the railway was the main interest, with the farthest accelerometer situated 45 m away. The subsequent tests concerned the vibration of the building and of the adjacent area. Figs. 6(c) and (d) present the locations of all sensors, the coordinates of which are listed in Table 4. For further details on the test, please refer to [30,31].

Table 3
The material and geometrical properties of the building, partially based on the test work [30].

Component	Material	Mass density ρ [kg/m^3]	Damping ratio η	V_p [m/s]	V_s [m/s]	Profile [m] Actual	Initial	Equivalent
Beam	Steel	7850	0.01	6000	3208	IPE 100 [39]	0.060/0.030	0.057/0.024
Pillar							0.080/0.080	0.093/0.067
Footing	Concrete	2500	0.01	3740	2290	0.7×0.7×0.35	–	–
Slab	Fiberboard	700	0.01	2619	1512	2.1×2.1×0.03	–	–

Table 4
The coordinates of monitoring points selected in this study.

Point	Coordinate [m]	Distance to railway [m]	Distance to building [m]	Location
S1	(0.0, 3.5, 0.0)	3.5	17.7	Ground surface
S2	(0.0, 7.0, 0.0)	7.0	14.2	
S3	(0.0, 15.0, 0.0)	15.0	6.2	
S4	(0.0, 22.5, 0.0)	22.5	1.3	
S5	(0.0, 9.2, 0.0)	9.2	12.0	
S6	(−3.5, 17.7, 0.0)	18.0	4.9	
M1	(2.2, 20.1, 0.0)	20.2	2.5	
P2	(0.0, 21.2, 2.0)	21.2	0.0	Floor slab
P21	(0.5, 20.7, 2.0)	20.7	0.0	

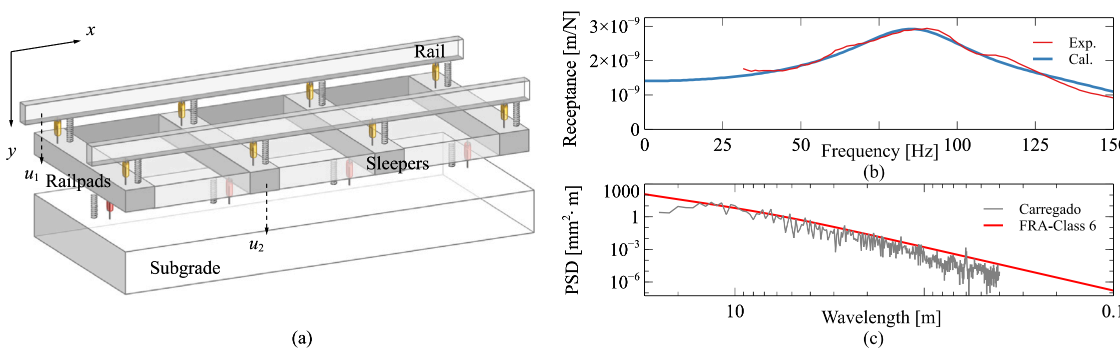

Fig. 2. The vehicle–track simulation: (a) the two-layer continuous model; (b) comparison of experimental and calculated rail cross receptances; (c) comparison of measured and FRA-Class 6 rail unevenness PSD data.

3. Methodology

The building is considerably away from the railway in the reference test, so it can hardly affect the production of train-induced perturbation [18]. In this study, the entire model is decoupled into vehicle–track and ground–building subsystems, interconnected by the load boundary conditions.

3.1. Vehicle–track sub-model

Moving vehicles induce perturbation on the ground surface, associated with the quasi-static and dynamic axle loads. Although the dominant frequency range of the latter falls outside that of structure response, they could affect vibrations at distant locations. Therefore, these two types of train-induced loads are determined and discussed.

We employ a 1D two-layer elastic model (Fig. 2(a)) to calculate the moving load on the ground surface. This model replaces the l-spacing sleepers with a continuous mass layer (m_s), while the springs and dashpots simulate the rail pads (k_p, c_p) and the underlying subgrade (k_b, c_b). A point load (P) with circular frequency ω_0 is applied on the sleeper according to the receptance test. The following equations govern the temporal (t) and spatial (x) responses of the rail (u_1) and sleepers (u_2) in the track system.

$$m_r \frac{\partial^2 u_1}{\partial t^2} + EI \frac{\partial^4 u_1}{\partial x^4} = -\left(k_p + c_p \frac{\partial}{\partial t}\right)(u_1 - u_2),$$
$$m_s \frac{\partial^2 u_2}{\partial t^2} = \left(k_p + c_p \frac{\partial}{\partial t}\right)(u_1 - u_2) - \left(k_b + c_b \frac{\partial}{\partial t}\right) u_2 + P e^{\mathrm{i}\omega_0 t} \delta(x), \quad (2)$$

where Dirac function $\delta(\cdot)$ defines the load location. In addition to two known rail pad parameters (k_p, c_p), manufacturers also provide the values (Table 5) for the rail mass per unit length (m_r) and its flexural stiffness (EI) [30]. In comparison, parameters of the subgrade (m_s, k_b, and c_b) are unknown and calibrated with the measured receptance $\alpha_e(\omega_0)$ by optimization [34].

By canceling the periodic factor $e^{\mathrm{i}\omega_0 t}$ and performing the Laplace transform (s is the transformed variable of x) to Eq. (2), the steady-state solution of rail cross receptance $\alpha(\omega_0)$ is a sum of residuals below [40]

$$\alpha(\omega_0) = \sum_{k=1}^{2} \mathrm{i}\,\mathrm{Res}\left(\frac{-F_p \exp(\mathrm{i}s_k l)}{L\left[F_p^2 - (F_p + F_r)(F_b + F_p + F_s)\right]}\right)\Bigg|_{\mathrm{Im}(s_k)>0}, \quad (3)$$

and

$$L = EI\,(k_p + k_b)/(k_p k_b),$$
$$F_p(k_p, c_p, \omega_0) = k_p + c_p \mathrm{i}\omega_0, \qquad F_b(k_b, c_b, \omega_0) = k_b + c_b \mathrm{i}\omega_0, \quad (4)$$
$$F_s(m_s, \omega_0) = -m_s\omega_0^2, \; F_r(EI, L, m_r, \omega_0, s_k) = EI s_k^4/L^4 - m_r\omega_0^2.$$

The calibration employs the least-squares objective function, namely $\sum\left(\alpha(\omega_{0,\,i}) - \alpha_e(\omega_{0,\,i})\right)^2$, within 150 Hz. Table 5 lists the related variable ranges and the initial/updated values. Note that these calibrated coefficients represent the equivalent properties of the ballast-subgrade subsystem. Fig. 2(b) compares the numerical/experimental receptances with good agreement achieved, which ensures the accuracy of the following train-induced load determination.

3.2. Train-induced loads

Firstly, considering the quasi-static axle loads, the moving perturbation induced by train vehicles with speed V_T can be obtained by series

Table 5
Calibrated track structure material properties.

Component	Parameter	Minimum/initial value	Maximum value	(Calibrated) value
Rail	m_r [kg/m]	–	–	60
	EI [Nm^2]	–	–	6.42×10^6
Railpad	$k_p l$ [N/m]	–	–	6.20×10^8
	$c_p l$ [Ns/m]	–	–	2.25×10^4
Sleeper-subgrade	$m_s l$ [kg]	1.00×10^2	1.00×10^4	1.36×10^3
	$k_b l$ [N/m]	1.00×10^6	1.00×10^9	4.30×10^8
	$c_b l$ [Ns/m]	1.00×10^3	1.00×10^6	3.50×10^5

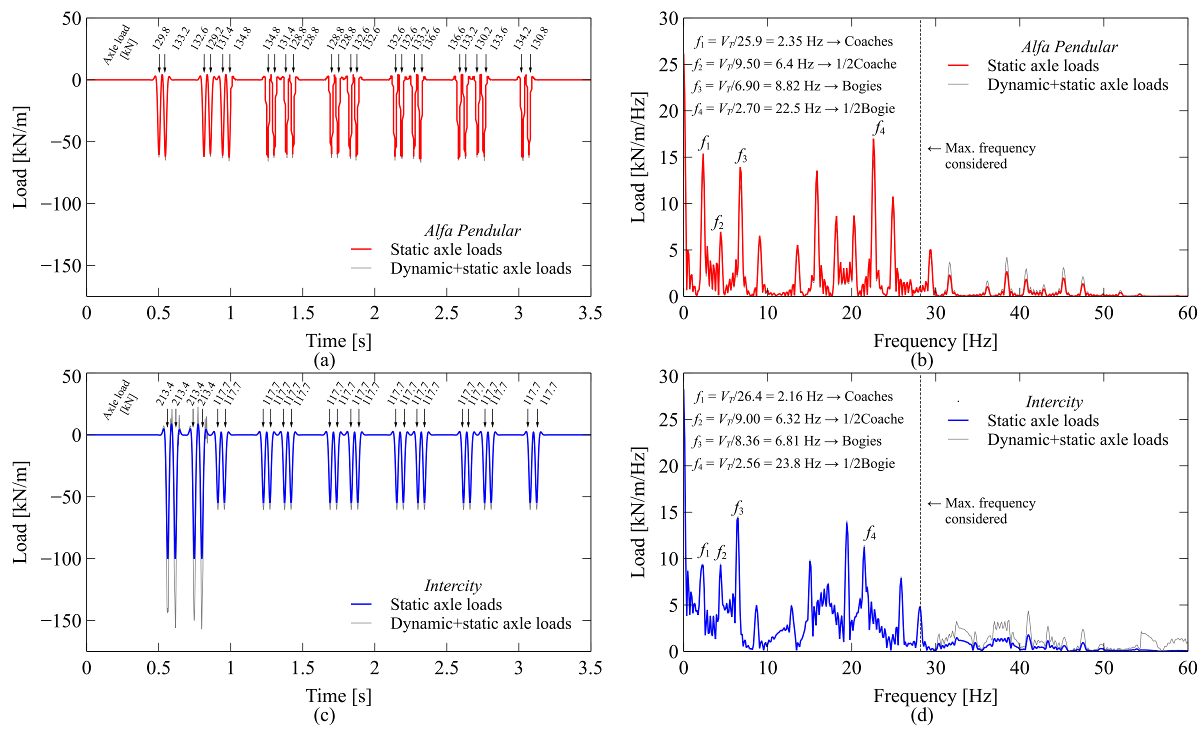

Fig. 3. The vehicle loads of two different trains: (a) time history and (b) Fourier spectrum of loads of Alfa Pendular moving at 219 km/h; (c) time history and (d) Fourier spectrum of loads of Intercity moving at 205 km/h.

expansion [41]. This method assumes that the displacement response (u_1, u_2) and the applied load (P) can be represented by their Fourier series within the moving reference frame ($\xi = x - V_T t$)

$$\begin{aligned} u_1(\xi) &= \frac{u_{1,0}}{2} + \sum_{i=1}^{+\infty} A_i \cos \Omega_i \xi + B_i \sin \Omega_i \xi, \\ u_2(\xi) &= \frac{u_{2,0}}{2} + \sum_{i=1}^{+\infty} C_i \cos \Omega_i \xi + D_i \sin \Omega_i \xi, \\ P(\xi) &= \frac{Q}{\lambda} + \sum_{i=1}^{+\infty} \frac{2Q}{\pi p i} \left[\sin \pi i - \sin\left(\pi i - \frac{\pi i p}{\lambda}\right)\right] \cos \Omega_i \xi, \\ \Omega_i &= 2\pi i/\lambda, \end{aligned} \tag{5}$$

where the axle load (Q) is related to the equivalent magnitude (P), influencing length (λ), and width (p).

Solving Eqs. (2) and (5) for coefficients A_i to D_i yields the moving perturbation F_T applied on the ground surface by n axles. The solution is expected to converge when a sufficiently large number of series terms is considered.

The steady-state moving perturbation F_T applied on ground surface induced by n axles has the following form

$$F_T(x,t) = F_T(x - V_T t) = \sum_{i=1}^{n} F_{T,\,i}(\xi) = \sum_{i=1}^{n} k_b u_{2,i}(\xi). \tag{6}$$

Secondly, based on the above 1D track model, the dynamic loads are determined by considering the interaction between rail and vehicles. The related coupled system is formulated by the general matrix equation with initial boundary conditions [42]

$$\begin{cases} \boldsymbol{M}\ddot{\boldsymbol{U}}(t) + \boldsymbol{C}\dot{\boldsymbol{U}}(t) + \boldsymbol{K}\boldsymbol{U}(t) = \boldsymbol{F}(t) \\ \boldsymbol{U}(0) = \boldsymbol{U}_0, \mathrm{d}\boldsymbol{U}(t)/\mathrm{d}t|_{t=0} = \boldsymbol{U}_0' \end{cases} \tag{7}$$

where, besides displacement $\boldsymbol{U}(t)$ and load $\boldsymbol{F}(t)$ vectors, $\boldsymbol{M}$, $\boldsymbol{C}$ and $\boldsymbol{K}$ stand for mass, damping, and stiffness matrices of the vehicle–track coupled system, respectively.

A verified code package, TTB-2D [43], is employed to calculate the transient solution of Eq. (7) based on train and rail properties available in [31]. The measured Power Spectral Density (PSD) of rail unevenness is presented in Fig. 2(c), showing better track quality compared to that of the Class-6 track recommended by FRA [44]. Therefore, the PSD of the Class-6 track is adopted in TTB-2D to calculate the dynamic axle loads.

Fig. 3 displays the train-induced loads of two types of vehicles in the time and frequency domain with wheel–rail contact considered or not. The dynamic interaction mainly amplifies the load components in the high-frequency range (greater than 30 Hz) and attenuates the lower ones. The differences between the two types of train-induced loads also highlight the role of the suspension systems, which is more evident for Alfa Pendular due to its better vibration isolation. It further suggests that, in this case study, quasi-static axle loads dominate train perturbation and can account for the resulting building vibrations characterized by lower natural frequencies illustrated in Section 3.3.

Additionally, in the frequency spectra of train-induced loads (Fig. 3) and also of ground motion (figures in Sections 4.2 and 4.3), several

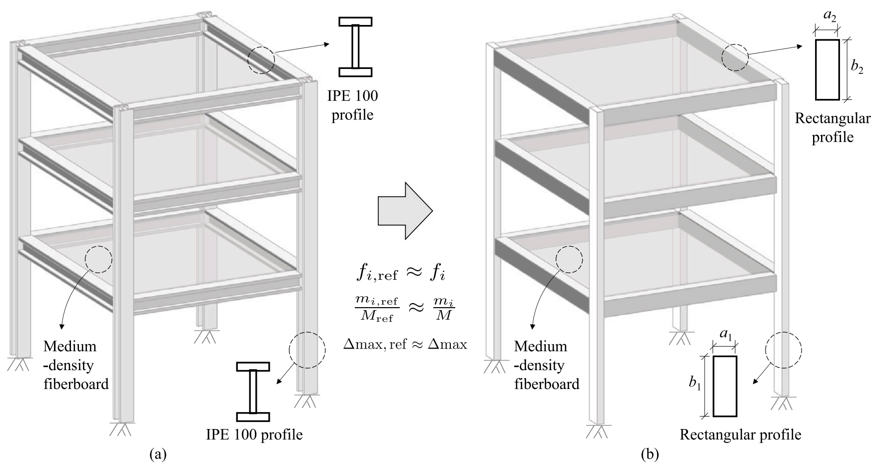

Fig. 4. (a) the actual/reference building constructed using a combination of IPE-100 steel beams and medium-density fiberboards; (b) the equivalent building fabricated with rectangular beams and medium-density fiberboards.

characteristic peaks are highlighted to illustrate the complex dependencies between train-induced loads and vehicle properties, including the lengths of bogies, coaches, and operating speed. Among these, high frequency (f_3, f_4) vibrations related to the distances of bogies are more influential at distant locations. A comparison between the train-induced perturbations of the two types of vehicles further reveals that the relative magnitudes of different axle loads (Figs. 3(a) and (c), Table 1) significantly affect the frequency distribution between peaks (Figs. 3(b) and (d)), which becomes more evident as the operating speed increases.

3.3. Ground–building sub-model

Compared to the vehicle–track interaction, the ground–foundation coupling is critical for the accuracy of the structure vibration prediction, as the SSI affects the overall dynamic properties. Regarding interaction simulation, non-conforming meshing, formulated by the Discontinuous Galerkin (DG) method [25], is utilized to address the numerical issues caused by the different spatial scales of ground and building elements. Fig. 1(b) shows the SEM model, where twenty DG pairs between the contacting faces have been introduced to accommodate portions of the numerical model with different size and polynomial order.

Given that the model building on site consists of beams and plates with small dimensions (IPE 100 steel beams and medium-density fiberboards detailed in Table 3 and Fig. 4(a)), its numerical modeling by SEM-based structural elements would face stability issues [45]. Since development of structural element libraries in SPEED and other SEM-based code packages [46,47] is still at a research progress, we decided to model the building by continuum spectral elements. In order to face the impractically small time steps required by numerical stability criteria, resulting from excessively small structural geometries, an equivalent building with comparable modal properties (Fig. 4(b)) was introduced. The material properties of such equivalent building are the same as those of the reference one, while its geometry is adjusted to make it feasible for the explicit time history analysis.

Fig. 5(a) illustrates the first eight natural frequencies of the reference steel structure. While the first to third modes involve either bending or torsional modes, the fourth to sixth ones are contributed by the vertical components (Fig. 5(c)). Modal mass ratios depicted in Fig. 5(b) confirm this observation. Searching for the equivalent building involves geometry-oriented optimization by iteratively adjusting cross-sections to minimize the differences in the modal properties. The following normalized non-linear optimization equations govern the entire procedure:

$$\begin{aligned} \min_{a_1,b_1,a_2,b_2} \quad & \sum_{i=1}^{8}\left[\frac{f_{i,\mathrm{ref}}-f_i}{f_{i,\mathrm{ref}}}\right]^2+\left[\frac{m_{i,\mathrm{ref}}/M_{\mathrm{ref}}-m_i/M}{m_{i,\mathrm{ref}}/M_{\mathrm{ref}}}\right]^2+\left[\frac{\Delta_{\mathrm{max,ref}}-\Delta_{\mathrm{max}}}{\Delta_{\mathrm{max,ref}}}\right]^2, \\ \text{subject to} \quad & a_j\in[0.75a_{j,0},\ 1.25a_{j,0}],\ (j=1,\ 2), \\ & b_k\in[0.75b_{k,0},\ 1.25b_{k,0}],\ (k=1,\ 2), \end{aligned} \tag{8}$$

where the feasible rectangular dimensions (a_1–b_2, labeled in Fig. 4(b)) of equivalent structure components satisfy the bounded constraints, and their initial values ($a_{j,0}$ and $b_{k,0}$) are found by equating the flexural stiffness to the reference one (detailed in Table 3). Apart from modal parameters (f and m/M), the objective function still includes the static indicator Δ_{max}, the maximum slab deflection to a unit load on the third floor.

We employ Isight [48], which provides unified process control by managing and directing multiple software in this study, like ABAQUS [49] and MATLAB [50], to conduct the above optimization. Table 3 presents the calibrated geometries of equivalent building components, whose modal parameters are depicted in Fig. 5 with those of the reference ones. It shows that the calibrated alternative building has similar vertical dynamic properties, although its transverse stiffness is slightly underestimated.

4. Numerical modeling and validation

4.1. SEM modeling

To reduce modeling complexity, we made some simplifying assumptions. For instance, the potential enhancement of soil properties around the building during construction is disregarded as well as the influence of soil poroelasticity, as the typical frequencies of soil vibration induced by the moving trains are much lower than the threshold for the onset of soil-fluid interaction [51]. Therefore, the soil response is represented by a linear visco-elastic model, with dynamic properties illustrated in Table 2.

We employ symmetry conditions along the mid-vertical plane (see Fig. 6(b)) to reduce the computational requirements. At the external borders, paraxial boundaries are applied to minimize spurious wave reflections. However, it is important to note that this numerical boundary is sensitive to the material Poisson's ratio ν, as it becomes unstable when ν exceeds 0.33 [52]. To avoid numerical instability, we added

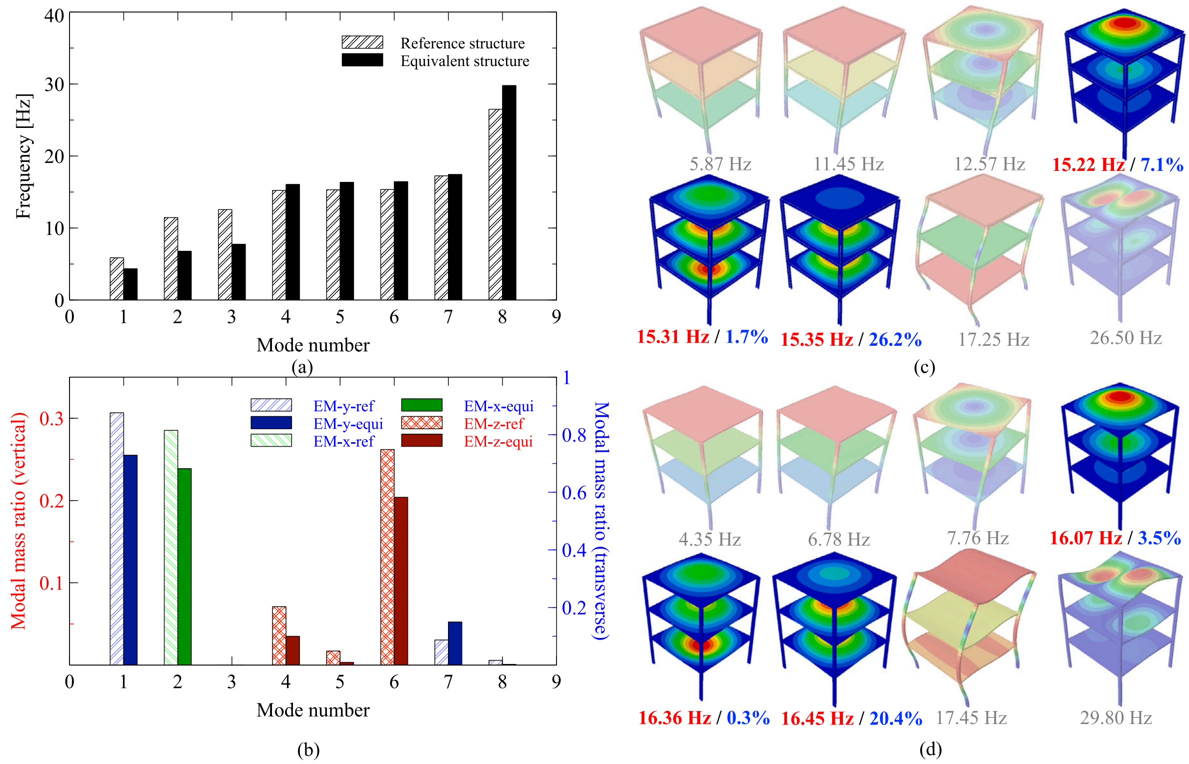

Fig. 5. Modal parameters of the actual building and the equivalent one: (a) the modal frequencies; (b) the modal mass ratios, EM-i, in three directions; (c) the mode shapes of the actual building; (d) the mode shapes of the equivalent one (labels are modal frequencies and vertical modal mass ratios).

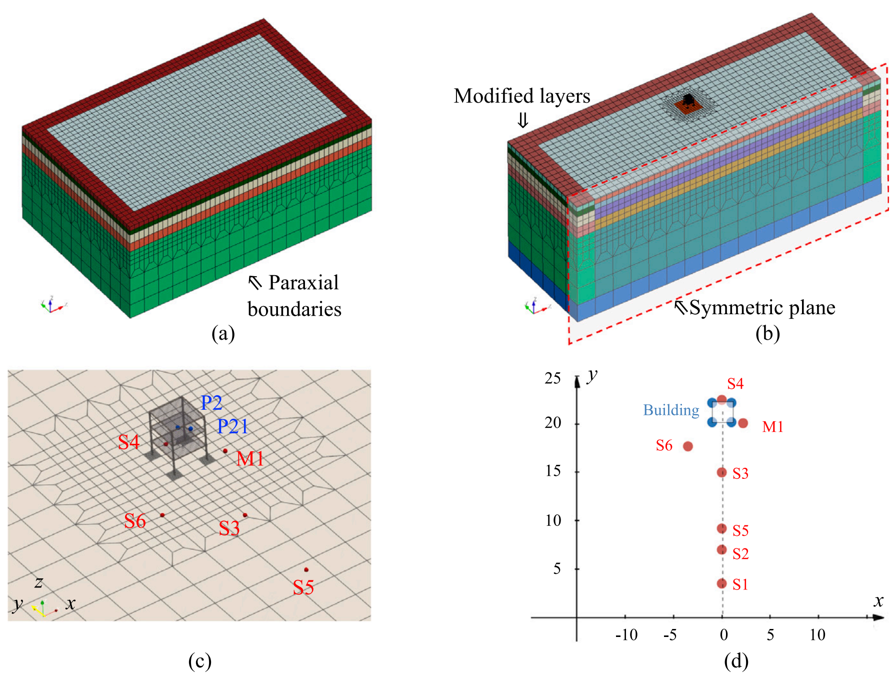

Fig. 6. The layouts of the 3D spectral element models: (a) ground model; (b) ground–building symmetric model; (c) spatial and (d) plan view of monitors (red/blue: ground/floor slab ones).

at the numerical model's edge a strip of elements with ν = 0.25 (see Figs. 6(a) and (b)). Compared to the analytical solutions, it is found that the potential effects on nearby areas are negligible (illustrated in Section 4.2).

We utilize the quadratic spectral elements for spatial discretization of the model, ensuring at least four grid points for the minimum wavelength [25]. As a result, an accurate simulation of wave propagation with frequencies up to 28 Hz is achieved. Figs. 6(a) and (b) present

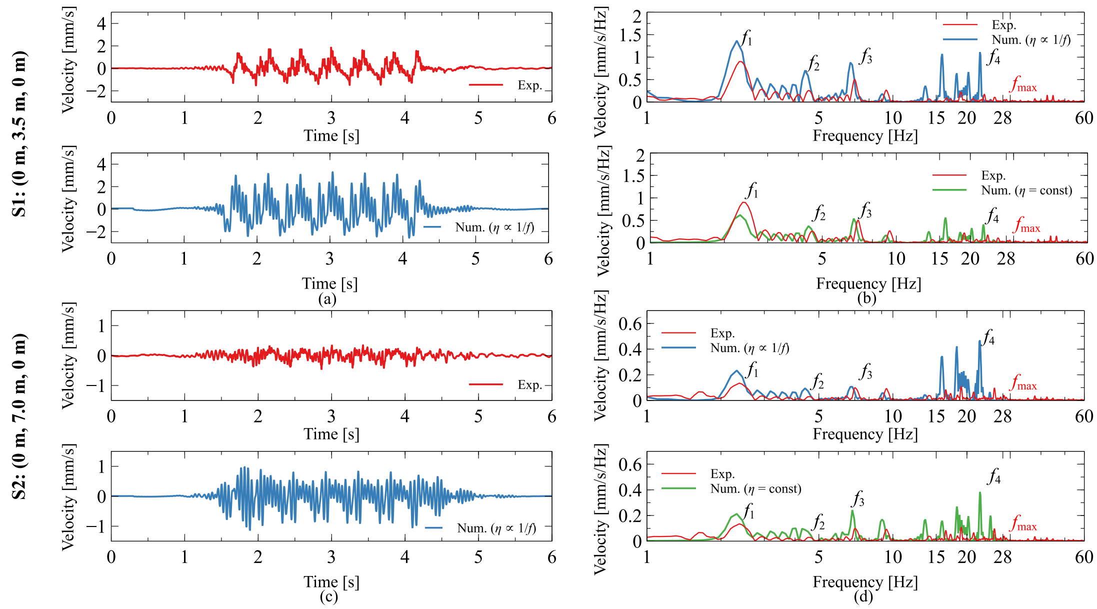

Fig. 7. Comparison of experimental and numerical vertical velocity responses at S1 (0, 3.5 m, 0) and S2 (0, 7 m, 0) under the passage of Alfa Pendular: (a) time histories and (b) Fourier spectra of S1 responses; (c) time histories and (d) Fourier spectra of S2 responses ($\eta \propto 1/f$ or $\eta = \text{const}$: models with proportional or constant damping.

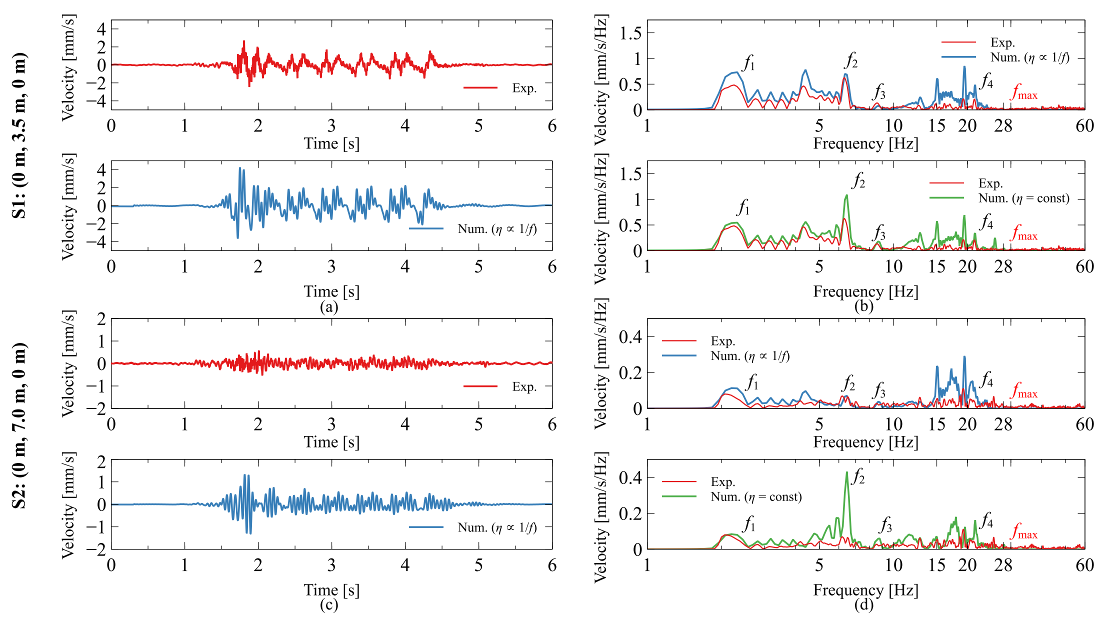

Fig. 8. Comparison of experimental and numerical vertical velocity responses at S1 (0, 3.5 m, 0) and S2 (0, 7 m, 0) under the passage of Intercity: (a) time histories and (b) Fourier spectra of S1 responses; (c) time histories and (d) Fourier spectra of S2 responses ($\eta \propto 1/f$ or $\eta = \text{const}$: models with proportional or constant damping.

the ground SEM and ground–building DG-SEM models, respectively, covering a total length of 100 m along the longitudinal direction.

4.2. Free-field vibration

Records of monitors outside the subgrade area are selected and compared to the experimental results, avoiding the computational singularity issues near the impacting locations. We apply band-pass filtering to all numerical results to retain components within the 2 to 28 Hz range. Regarding the test records, high-pass filtering is applied to reserve components with a frequency over 1.5 Hz. Figs. 7 and 8 illustrate the vertical velocity responses induced by Alfa Pendular and Intercity at S1 and S2, 3.5 m and 7.0 m away from the track, respectively.

Numerical results in Fig. 7 show a slightly amplified prediction. Similar component distribution is reproduced in the low-frequency range, while the discrepancies in the high-frequency range indicate the damping complexity of geomaterials. A sensitivity study was made to assess the effects of soil damping: namely two typical damping patterns are considered, i.e. the frequency proportional and constant damping ones, and numerical results are provided in Figs. 7–10, panels (b) and (d). It is found that constant damping provides a closer prediction in the high-frequency domain but overestimates in the lower range. In the case of Intercity depicted in Fig. 8, the comparison exhibits a better agreement, especially in the low-frequency range. It suggests that the predictions obtained by the proportional damping are more suitable for reproducing vibration properties.

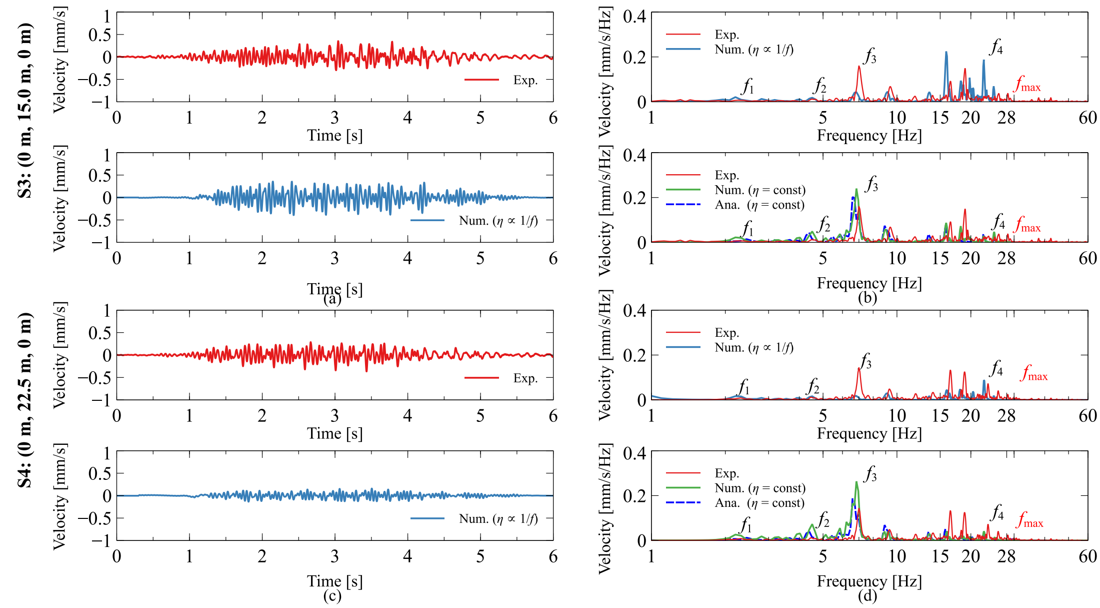

Fig. 9. Comparison of experimental, numerical and, analytical vertical velocity responses at S3 (0, 15 m, 0) and S4 (0, 22.5 m, 0) under the passage of Alfa Pendular: (a) time histories and (b) Fourier spectra of S3 responses; (c) time histories and (d) Fourier spectra of S4 responses ($\eta \propto 1/f$ or $\eta = \text{const}$: models with proportional or constant damping.

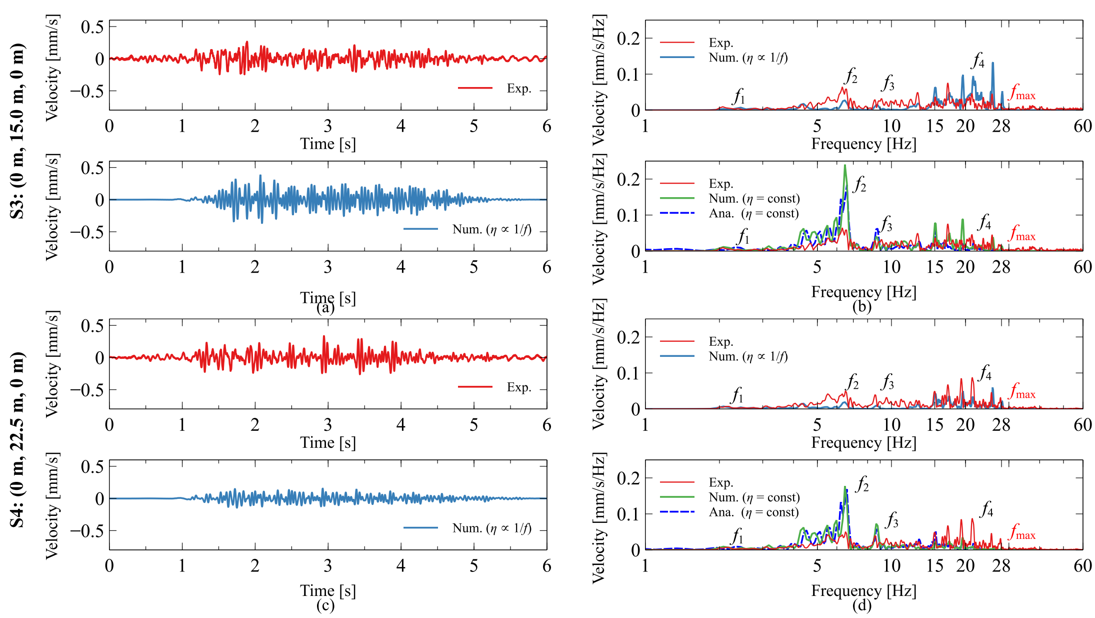

Fig. 10. Comparison of experimental, numerical and, analytical vertical velocity responses at S3 (0, 15 m, 0) and S4 (0, 22.5 m, 0) under the passage of Intercity: (a) time histories and (b) Fourier spectra of S3 responses; (c) time histories and (d) Fourier spectra of S4 responses ($\eta \propto 1/f$ or $\eta = \text{const}$: models with proportional or constant damping.

Furthermore, it is also shown in Figs. 7–10 that the Fourier spectra of records are larger at lower frequencies. As the frequency exceeds 28 Hz, i.e., the maximum effective frequency considered in the numerical simulation, the impact of these experimental results becomes less pronounced. This observation reinforces the idea that, in this case study, the primary contribution comes from the quasi-static axle loads.

Figs. 9 and 10 illustrate the responses at S3 and S4, 15 m and 22.5 m away from the test line, for two types of trains. The observed variation in the vibration decline compared to S1 and S2 within the concerned frequency range underscores the intricate nature of soil damping and the heterogeneity of the soil conditions. Upon evaluating the differences in prediction using two damping patterns with the records, it becomes evident that the prediction under proportional damping behaves better than the constant one. Besides, ground vibrations are also calculated analytically at these locations near the model boundaries through the Betti–Rayleigh dynamic reciprocity theorem [23]. The Fourier spectra of the numerical results depicted in Figs. 9 and 10 exhibit a remarkable agreement with the analytical ones, providing strong verification for the adopted scheme for the absorbing boundaries.

In addition, Fig. 11 shows the calculated PGV (Peak Ground Velocity) curves along the center line, which are closely associated with the amplitude of train-induced loads. However, despite having higher initial values due to heavy axle loads (see Fig. 3), Intercity-induced

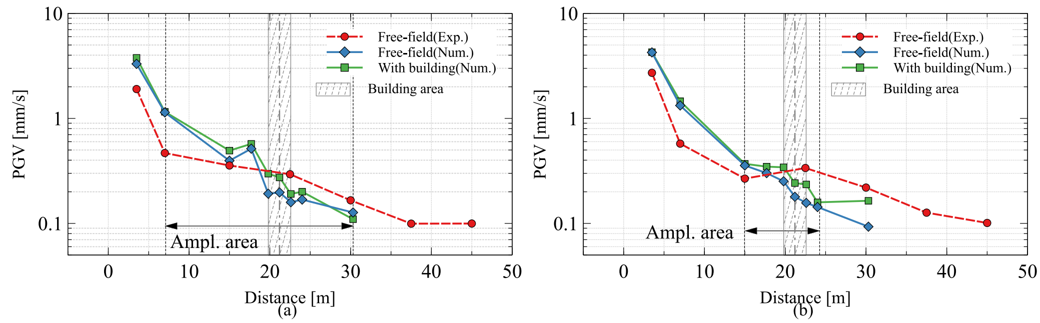

Fig. 11. Comparison of experimental and numerical peak ground velocity along the transverse direction with or without the building: (a) by Alfa Pendular; (b) by Intercity.

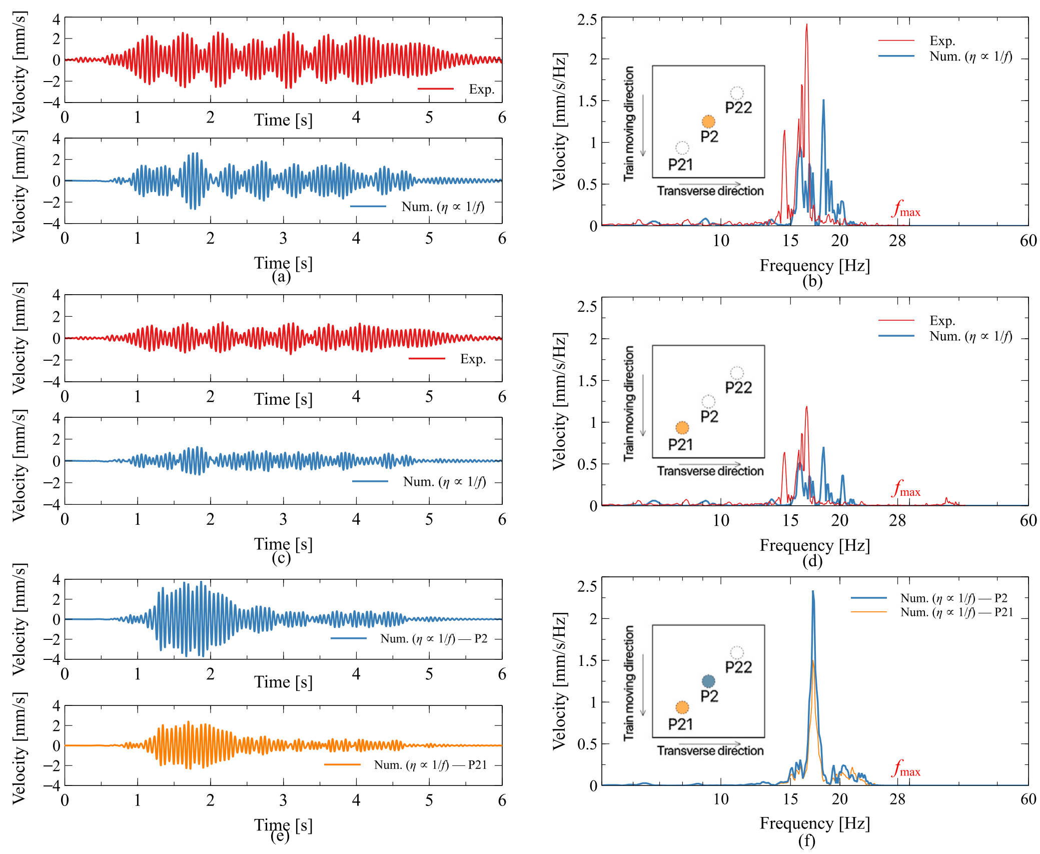

Fig. 12. Comparison of experimental and numerical slab responses at P2 (0, 21.2 m, 2.0 m) and P21 (0, 20.7 m, 2.0 m). Alfa Pendular case: (a) time and (b) Fourier domain of P2 responses; (c) time and (d) Fourier domain of P21 responses; Intercity case: (e) time and (f) Fourier domain of P2, P21 responses ($\eta \propto 1/f$: model with proportional damping).

vibrations decay faster than those of Alfa Pendular. The variation in decline levels is linked to the values of the vehicle intervals. Specifically, smaller intervals of Intercity trains give rise to waves propagating with higher frequencies, resulting in a more rapid attenuation. This correlation indicates the significant influence of vehicle spacing on the frequency and attenuation characteristics of train-induced vibrations.

4.3. Building–ground vibration

Various locations (Fig. 6(d)) within and around the building are examined. Figs. 12(a–d) compare the velocity responses induced by Alfa Pendular at two points (P2, P21) on the second-floor slab. The numerical/experimental time history results (see Figs. 12(a) and (c)) exhibit similar oscillating patterns with consistent amplitudes.

Frequency analyses (see Figs. 12(b) and (d)) provide more insights into the prediction of slab vibrations. We can observe a rightward translation of nearly 2 Hz in the frequencies of three activated bending modes in the numerical results compared to the experimental ones. The discrepancy in the results stems from the less precise characterization of the equivalent building concerning its modal frequencies (Fig. 5(a)). This imprecision further amplifies secondary deviations in the vibration magnitudes. However, the primary oscillating properties of responses at the concerned locations are reproduced with minor discrepancies in the numerical predictions, confirming the model's reliability. The exam of Fourier spectra further reveal a reduction of coupled natural frequencies attributed to the soil's absorbing properties. In the case of Intercity, Figs. 12(e) and (f) present that, in addition to the higher vibrations induced by its locomotive, the slab undergoes oscillations characterized by one dominant mode at all positions. Compared to Alfa Pendular-induced multiple modal responses, this distinction is closely associated with the train geometry properties.

In what concerns the ground motion in the presence of the building, three typical monitoring locations (M1, S6, and S5) are selected at varying distances from the structure (labeled as r on the left margin

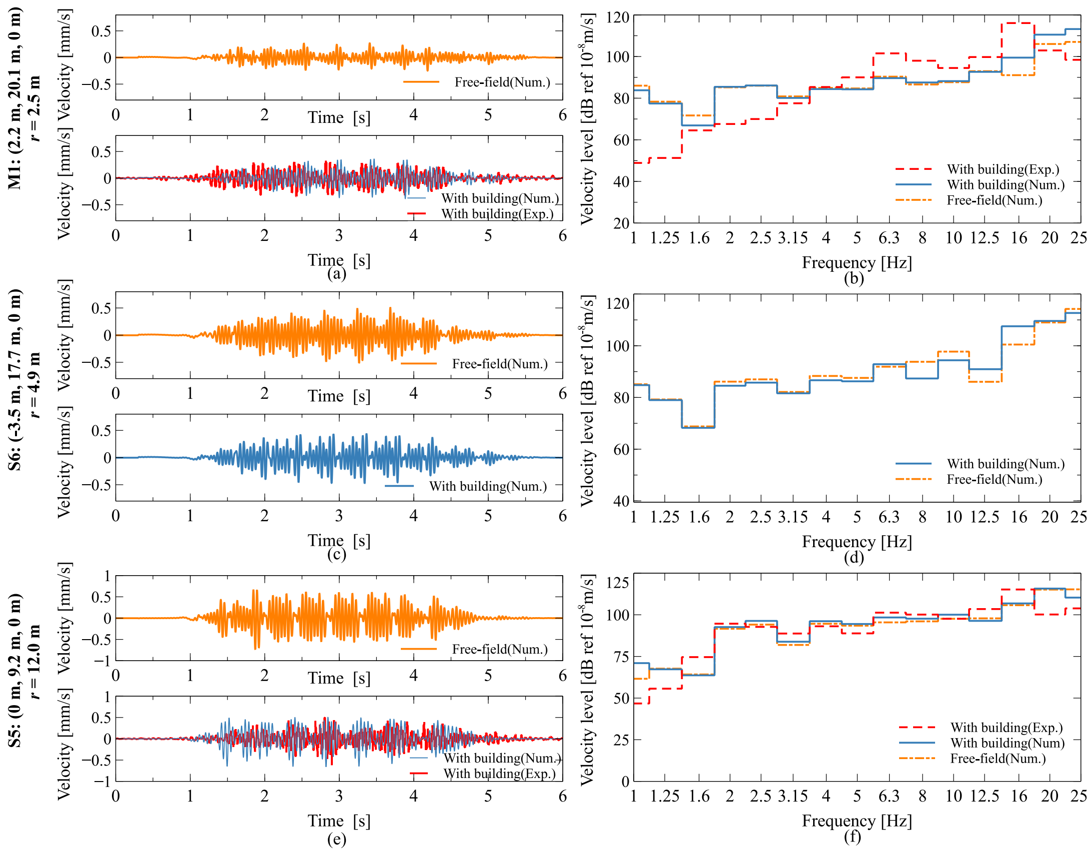

Fig. 13. Comparison of experimental and numerical vertical velocity responses with or without the building at M1 (r = 2.5 m), S6 (r = 4.9 m) and S5 (r = 12.0 m) under the passage of Alfa Pendular: (a) time histories and (b) Fourier spectra of M1 responses; (c) time histories and (d) Fourier spectra of S6 responses; (e) time histories and (f) Fourier spectra of S5 responses.

of figures). The time history responses shown in Figs. 13(a–e) of the Alfa Pendular case indicate that the amplification occurs within an area very close to the building. The results in the frequency domain are transformed into velocity levels ($L_v = 20\log_{10}(V_{\mathrm{RMS}}/V_{\mathrm{ref}})$) in the one-third octave band, as depicted in Figs. 13(b–f). It is shown that the presence of the model building primarily interferes with the nearby ground vibrations through its bending modes (around 15 Hz). However, Fig. 13(f) presents that this influence decreases at more distant locations, such as S5 (12 m away). Further comparison in the Intercity case (Fig. 14) reveals that the above SSI effect is sensitive to the vehicle properties. Unlike high-speed trains, vibrations to Intercity passages are not evidently amplified in the concerned frequency range (of the slab modes) with the presence of structure.

Moreover, the PGV curves in Fig. 11 also include the cases considering the presence of the building. Compared to the free-field motion, vibrations within the building area induced by both train passages are consistently amplified. The effect is more pronounced in the front rather than in the rear zone, possibly due to the additional wave reflections. Concerning the affected range, it is observed that the vibration amplification area caused by Alfa Pendular is broader than that of Intercity (marked in Fig. 11). This difference further suggests the influences of vehicle properties on the coupling vibrations of ground and building.

5. Conclusions

To handle the numerical challenges posed by coupling the multi-scale modeling components in train-induced ground and building vibration prediction, the spectral element method, implemented in the code SPEED (https://speed.mox.polimi.it/) and enhanced by a discontinuous Galerkin formulation, is confirmed as a promising numerical alternative to FEM, because of its spectral convergence properties. The performance of the approach was validated through an existing field test, carried out in Portugal [30,31], including records on ground and prototype building with different types of train passage. For this purpose, the vehicle–track system was first decoupled, and the computed loading of the moving train was applied to a 3D numerical model representing the ground–building subsystem. Equivalent building properties were identified to simplify the numerical model and reduce the computational burden. Some sensitivity studies concerning the effects of SSI and vehicle properties were also carried out. The following conclusions are drawn:

(1) the coupled ground–building SEM 3D model, with equivalent building cross-section, demonstrates sufficient capability in simulating the recorded motion for the different experimental case studies, showing that the main mechanisms of HSR-induced ground and building vibrations are well captured, as well as their coupling effects;
(2) the presence of the scale model building, in this case study, amplifies the ground motion in adjacent areas mainly due to the local resonances of floor slabs. The vibration amplification area in front of the building is broader than behind it, primarily caused by the wave reflections ahead of the footings;
(3) despite the comparable operating speed levels, the vehicle properties, such as axle loads and intervals, are found to influence ground motion and the range of the vibration amplification area by activating different modes of the ground–building coupled system.

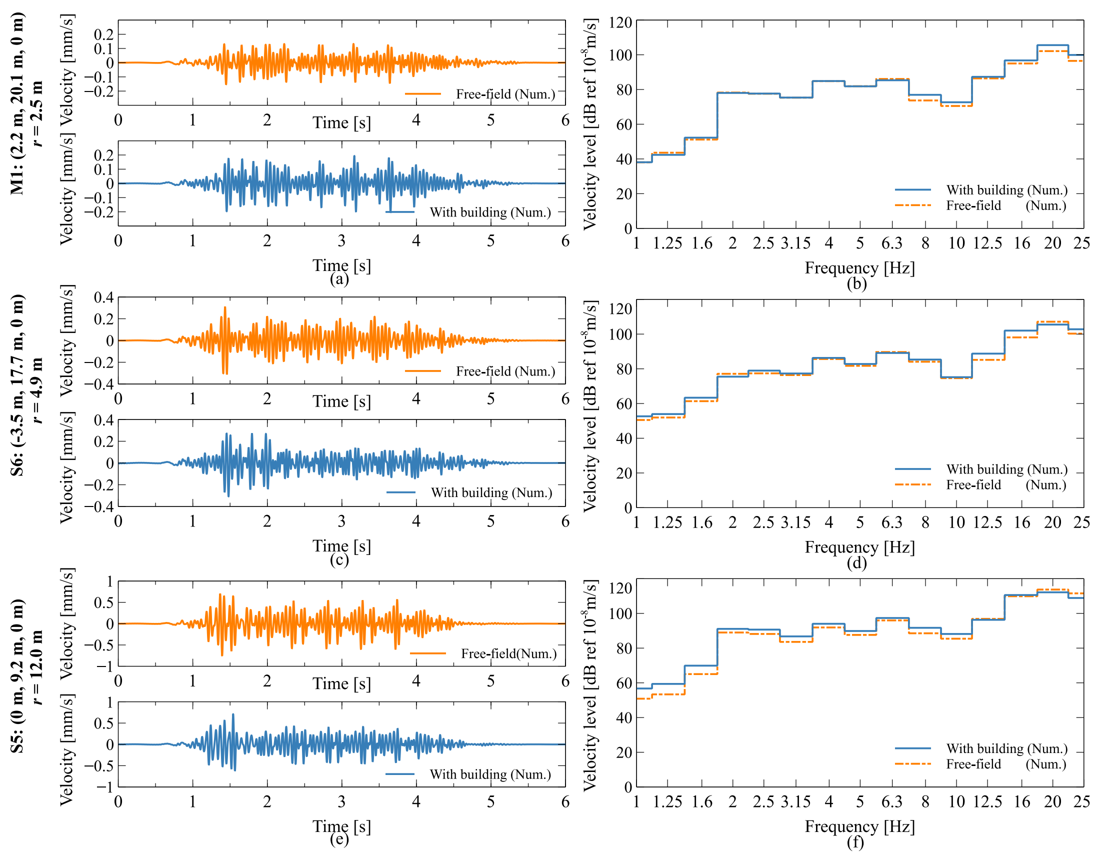

Fig. 14. Comparison of numerical vertical velocity responses with or without the building at M1 (r = 2.5 m), S6 (r = 4.9 m) and S5 (r = 12.0 m) under the passage of Intercity: (a) time histories and (b) Fourier spectra of M1 responses; (c) time histories and (d) Fourier spectra of S6 responses; (e) time histories and (f) Fourier spectra of S5 responses.

CRediT authorship contribution statement

Duo Feng: Writing – original draft, Software, Methodology, Investigation. **Roberto Paolucci:** Writing – review & editing, Supervision, Resources, Conceptualization. **Ilario Mazzieri:** Software, Methodology. **Linrong Xu:** Resources, Conceptualization. **Yu Cai:** Writing – review & editing, Resources.

Declaration of competing interest

The authors declare that they have no known competing financial interests or personal relationships that could have appeared to influence the work reported in this paper.

Data availability

Data will be made available on request.

Acknowledgments

The authors are grateful to Prof. Aires Colaço for kindly providing the supplementary and detailed test data of the Carregado field experiment. We thank the help of Srihari Sangaraju for his suggestions on spectral element modeling. We appreciate the comments made by four anonymous reviewers, which substantially improved the quality of this manuscript.

This work was supported by the China Scholarship Council (Grant No. 202106370077); CINECA HPC project (ISCRA B SSI-RISK); National Natural Science Foundation of China (Grant No. 42172322); and Hunan Provincial Natural Science Foundation, China (Grant No. 21B0179).

References

[1] Kim Minho, Chang Seo I, Seong Jeong C, Holt James B, Park Tae H, Ko Joon H, Croft Janet B. Road traffic noise: annoyance, sleep disturbance, and public health implications. Am J Prev Med 2012;43(4):353–60.

[2] Jik Lee Pyoung, Griffin Michael J. Combined effect of noise and vibration produced by high-speed trains on annoyance in buildings. J Acoust Soc Am 2013;133(4):2126–35.

[3] Ropars Pierre, Vuylsteke Xavier, Augis Eric. Vibrations induced by metro in sensitive buildings; experimental and numerical comparisons. In: EURONOiSE 2018 conference. Heraklion, Greece. 2018, p. 1381–6.

[4] Wang Sen, Xin Tao, Wang Pengsong, Yang Yi, Zhao Lei. Assessment and mitigation of railway-induced environmental vibrations over underground comprehensive transportation hub. Struct Infrastruct Eng 2022;1–12.

[5] Li Xuming, Chen Yekai, Zou Chao, Wu Junhuan, Shen Zixiong, Chen Ying. Building coupling loss measurement and prediction due to train-induced vertical vibrations. Soil Dyn Earthq Eng 2023;164:107644.

[6] Hu Zihao, Tian Li, Zou Chao, Wu Jie. Train-induced vibration attenuation measurements and prediction from ground soil to building column. Environ Sci Pollut Res 2023;1–17.

[7] Connolly David P, Kouroussis Georges, Laghrouche Omar, Ho CL, Forde MC. Benchmarking railway vibrations–Track, vehicle, ground and building effects. Constr Build Mater 2015;92:64–81.

[8] Waller RA. Building on springs. International series of monographs in civil engineering, first edn. Pergamon Press; 1969.

[9] Hunt HEM. Stochastic modelling of traffic-induced ground vibration. J Sound Vib 1991;144(1):53–70.

[10] Hunt HEM. Prediction of vibration transmission from railways into buildings using models of infinite length. Veh Syst Dynam 1995;24(sup1):234–47.

[11] Balendra T, Koh CG, Ho YC. Dynamic response of buildings due to trains in underground tunnels. Earthq Eng Struct Dynam 1991;20(3):275–91.

[12] Fiala P, Degrande Geert, Augusztinovicz F. Numerical modelling of ground-borne noise and vibration in buildings due to surface rail traffic. J Sound Vib 2007;301(3–5):718–38.

[13] Connolly David P, Galvín Pedro, Olivier Bryan, Romero Antonio, Kouroussis Georges. A 2.5 D time-frequency domain model for railway induced soil-building vibration due to railway defects. Soil Dyn Earthq Eng 2019;120:332–44.

[14] Sanayei Masoud, Zhao Ningyu, Maurya Pradeep, Moore James A, Zapfe Jeffrey A, Hines Eric M. Prediction and mitigation of building floor vibrations using a blocking floor. J Struct Eng 2012;138(10):1181–92.
[15] Zou Chao, Moore James A, Sanayei Masoud, Wang Yimin. Impedance model for estimating train-induced building vibrations. Eng Struct 2018;172:739–50.
[16] Pyl Lincy, Degrande Geert, Lombaert Geert, Haegeman Wim. Validation of a source–receiver model for road traffic-induced vibrations in buildings. I: Source model. J Eng Mech 2004;130(12):1377–93.
[17] Pyl Lincy, Degrande Geert, Clouteau Didier. Validation of a source–receiver model for road traffic-induced vibrations in buildings. II: Receiver model. J Eng Mech 2004;130(12):1394–406.
[18] Coulier Pieter, Lombaert Geert, Degrande Geert. The influence of source–receiver interaction on the numerical prediction of railway induced vibrations. J Sound Vib 2014;333(12):2520–38.
[19] Faccioli Ezio, Maggio Fabio, Paolucci Roberto, Quarteroni Alfio. 2D and 3D elastic wave propagation by a pseudo-spectral domain decomposition method. J Seismol 1997;1:237–51.
[20] Paolucci Roberto, Faccioli Ezio, Maggio Fabio. 3D response analysis of an instrumented hill at Matsuzaki, Japan, by a spectral method. J Seismol 1999;3:191–209.
[21] Paolucci Roberto. Amplification of earthquake ground motion by steep topographic irregularities. Earthq Eng Struct Dynam 2002;31(10):1831–53.
[22] Paolucci Roberto, Maffeis Andrea, Scandella Laura, Stupazzini Marco, Vanini Manuela. Numerical prediction of low-frequency ground vibrations induced by high-speed trains at Ledsgaard, Sweden. Soil Dyn Earthq Eng 2003;23(6):425–33.
[23] Paolucci Roberto, Spinelli Davide. Ground motion induced by train passage. J Eng Mech 2006;132(2):201–10.
[24] Stupazzini M, Paolucci R. Ground motion induced by train passage in urban area. In: ISMA2010 international conference on noise and vibration engineering. 2010, p. 20–2.
[25] Mazzieri Ilario, Stupazzini Marco, Guidotti Roberto, Smerzini Chiara. SPEED: Spectral elements in elastodynamics with discontinuous Galerkin: A non-conforming approach for 3D multi-scale problems. Internat J Numer Methods Engrg 2013;95(12):991–1010.
[26] Kato Bence, Wang Gang. Seismic site–city interaction analysis of super-tall buildings surrounding an underground station: a case study in Hong Kong. Bull Earthq Eng 2022;20(3):1431–54.
[27] Fares Reine, Castro Cruz David, Foerster Evelyne, Lopez-Caballero Fernando, Gatti Filippo. Coupling spectral and Finite Element methods for 3D physic-based seismic analysis from fault to structure: Application to the Cadarache site in France. Nucl Eng Des 2022;397:111954.
[28] Lu Xinzheng, Tian Yuan, Wang Gang, Huang Duruo. A numerical coupling scheme for nonlinear time history analysis of buildings on a regional scale considering site-city interaction effects. Earthq Eng Struct Dynam 2018;47(13):2708–25.
[29] Tian Yuan, Lu Xinzheng, Huang Duruo, Wang Tao. SCI effects under complex terrains: Shaking table tests and numerical simulation. J Earthq Eng 2023;27(5):1237–60.
[30] Colaço Aires, Costa Pedro Alves, Castanheira-Pinto Alexandre, Amado-Mendes Paulo, Calçada Rui. Experimental validation of a simplified soil-structure interaction approach for the prediction of vibrations in buildings due to railway traffic. Soil Dyn Earthq Eng 2021;141:106499.
[31] Dos Santos N Correia, Colaço A, Costa P Alves, Calçada R. Experimental analysis of track-ground vibrations on a stretch of the portuguese railway network. Soil Dyn Earthq Eng 2016;90:358–80.
[32] Colaço A, Castanheira-Pinto A, Alves Costa P, Fernández Ruiz J. Combination of experimental measurements and numerical modelling for prediction of ground-borne vibrations induced by railway traffic. Constr Build Mater 2022;343:127928.
[33] Costa P Alves, Calçada R, Cardoso A Silva. Track-ground vibrations induced by rail traffic. 2012.
[34] Costa P Alves, Calçada Rui, Cardoso A Silva. Track–ground vibrations induced by railway traffic: In-situ measurements and validation of a 2.5 D FEM-BEM model. Soil Dyn Earthq Eng 2012;32(1):111–28.
[35] Dos Santos N Correia, Barbosa J, Calçada R, Delgado R. Track-ground vibrations induced by railway traffic: experimental validation of a 3D numerical model. Soil Dyn Earthq Eng 2017;97:324–44.
[36] Colaço Aires, Costa Pedro Alves, Amado-Mendes Paulo, Calçada Rui. Vibrations induced by railway traffic in buildings: Experimental validation of a sub-structuring methodology based on 2.5 D FEM-MFS and 3D FEM. Eng Struct 2021;240:112381.
[37] Anbazhagan P, Uday Anjali, Moustafa Sayed SR, Al-Arifi Nassir SN. Correlation of densities with shear wave velocities and SPT N values. J Geophys Eng 2016;13(3):320–41.
[38] Colaço Aires Manuel Silva. Vibrações e ruído estrutural induzidos por tráfego ferroviário: modelação numérica integrada e validação experimental (Ph.D. thesis), University of Porto; 2019.
[39] Vayas Ioannis, Ermopoulos John, Ioannidis George. Design of steel structures to eurocodes. Springer International Publishing; 2019, http://dx.doi.org/10.1007/978-3-319-95474-5,
[40] Grassie SL, Gregory RW, Harrison D, Johnson KL. The dynamic response of railway track to high frequency vertical excitation. J Mech Eng Sci 1982;24(2):77–90.
[41] Czyczula Wlodzimierz, Koziol Piotr, Kudla Dariusz, Lisowski Sergiusz. Analytical evaluation of track response in the vertical direction due to a moving load. J Vib Control 2017;23(18):2989–3006.
[42] Zhai Wanming, Zhai Wanming. Vehicle–track coupled dynamics models. Springer; 2020.
[43] Cantero Daniel. TTB-2D: Train–Track–Bridge interaction simulation tool for matlab. SoftwareX 2022;20:101253.
[44] Frỳba Ladislav. Dynamics of railway bridges. Thomas Telford Publishing; 1996.
[45] Zuchowski Loïc, Brun Michael, De Martin Florent. Co-simulation coupling spectral/finite elements for 3D soil/structure interaction problems. C R Mec 2018;346(5):408–22.
[46] Komatitsch Dimitri, Peter Daniel, Durochat Clément, Monteiller Vadim, Zhinan Xie, 1sbeller, Aakash Gupta, Ampuero Jean Paul, Modrak Ryan, Weng Huihui, Casarotti Emanuele, VmontLma, Morency Christina, Gassmoeller Rene, Heien Eric, Tape Carl, Bottero, Luet David, Nagaso Masaru, Kangchen Bai, McBain GD, Oral Elif, Cano Eduardo Valero, Bissey François, Miller David, Almada Rafael, Buildbot-Princeton, EtienneBachmann, Minchenatrice, Karakostas Foivos. SPECFEM/specfem3d: SPECFEM3D v4.0.0. 2023, http://dx.doi.org/10.5281/ZENODO.7734075.
[47] Ampuero Jean-Paul. A spectral element method tool for 2D wave propagation and earthquake source dynamics user's guide. 2012.
[48] Simulia Isight. ISIGHT users' guide. Dassault Syst 2016.
[49] CAE User. ABAQUS 6.14 analysis user guide. Dassault Syst 2014.
[50] The MathWorks Inc.. MATLAB version: 9.13.0 (R2022b). Natick, Massachusetts, United States: The MathWorks Inc.; 2022, URL https://www.mathworks.com.
[51] Schevenels Mattias, Degrandec G, Lombaert Geert. The influence of the depth of the ground water table on free field road traffic-induced vibrations. Int J Numer Anal Methods Geomech 2004;28(5):395–419.
[52] Kausel Eduardo. Physical interpretation and stability of paraxial boundary conditions. Bull Seismol Soc Am 1992;82(2):898–913.